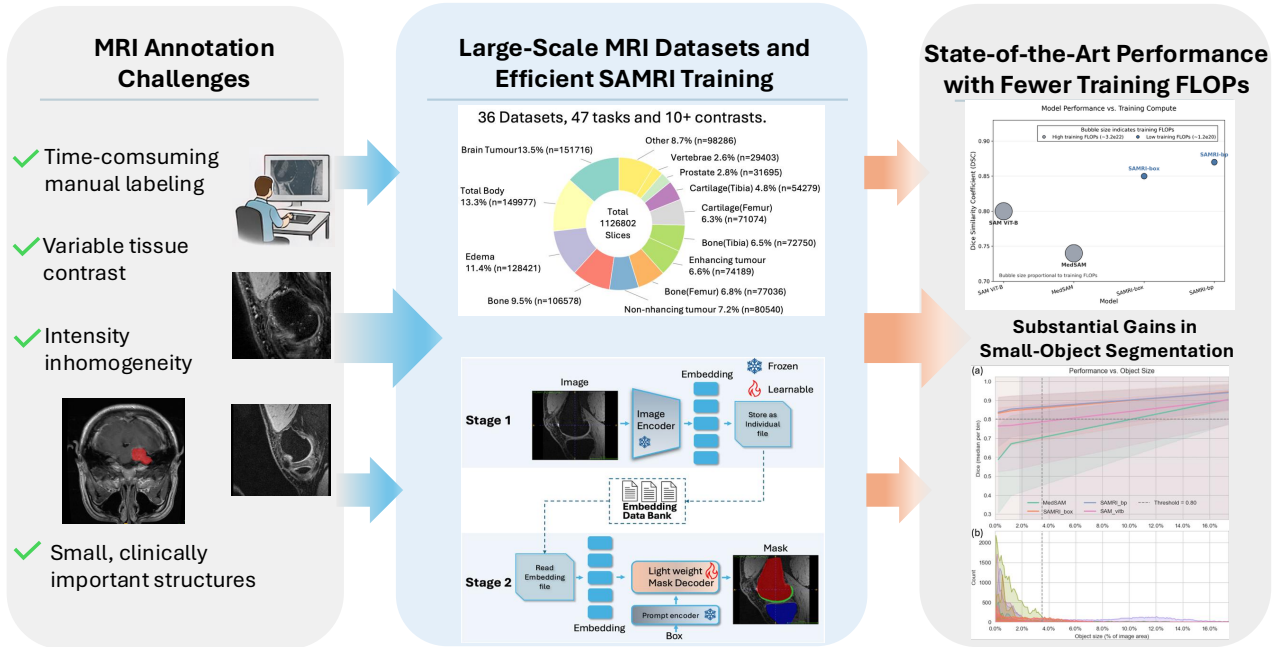


Graphical Abstract

SAMRI: Segment Anything Model for MRI

Zhao Wang, Wei Dai, Thuy Thanh Dao, Steffen Bollmann, Hongfu Sun, Craig Engstrom, Shekhar S. Chandra

arXiv:2510.26635v2 [eess.IV] 23 Jan 2026



Highlights

SAMRI: Segment Anything Model for MRI

Zhao Wang, Wei Dai, Thuy Thanh Dao, Steffen Bollmann, Hongfu Sun, Craig Engstrom, Shekhar S. Chandra

- Large-scale MRI adaptation of SAM trained on 1.1M slices across 47 tasks and 10+ contrasts.
- Addresses the "small object" failure mode in medical foundation models with substantial gains on clinically significant structure.
- Achieves state-of-the-art accuracy and robust zero-shot generalization across diverse, unseen MRI targets.
- Novel two-stage training reduces FLOPs cost by over 99%, enabling large-scale training on consumer GPUs.
- End-to-end practical deployment pipeline featuring an open-source, interactive local GUI.

SAMRI: Segment Anything Model for MRI

Zhao Wang^{a,*}, Wei Dai^a, Thuy Thanh Dao^a, Steffen Bollmann^{a,b}, Hongfu Sun^c, Craig Engstrom^d, Shekhar S. Chandra^a

^a*School of Electrical Engineering and Computer Science, The University of Queensland, Australia*

^b*Queensland Digital Health Centre, University of Queensland, Australia*

^c*School of Engineering, College of Engineering, Science and Environment, University of Newcastle, Australia*

^d*School of Human Movement and Nutrition Sciences, The University of Queensland, Australia*

Abstract

Accurate magnetic resonance imaging (MRI) segmentation is crucial for clinical decision-making, but remains labor-intensive when performed manually. Convolutional neural network (CNN)-based methods can be accurate and efficient but often generalize poorly to MRI’s variable contrast, intensity inhomogeneity, and sequences. Although the transformer-based Segment Anything Model (SAM) has demonstrated remarkable generalizability in natural images, existing adaptations often treat MRI as another imaging modality, overlooking these modality-specific challenges. We present SAMRI, an MRI-specialized SAM trained and validated on 1.1 million labeled MR slices spanning whole-body organs and pathologies. We demonstrate that SAM can be effectively adapted to MRI by fine-tuning its mask decoder using a two-stage strategy, reducing training time by 94% and trainable parameters by 96% compared to full-model retraining. Across diverse MRI segmentation tasks, SAMRI achieves a mean Dice of 0.87, delivering state-of-the-art accuracy across anatomical regions and robust generalization on unseen structures, particularly small clinically important structures. In addition, we provide a complete training-to-inference pipeline and a user-friendly local graphical interface that enables interactive application of pretrained SAMRI models on standard machines, facilitating practical deployment for real-world MRI segmentation. Code and models are available at: <https://github.com/wangzhaomxy/SAMRI>

Keywords: MRI, Segmentation, SAM, Vision Transformer, Small object, Deep learning, Whole body

1. Introduction

Magnetic resonance imaging (MRI) provides exquisite soft-tissue visualization, making it well suited for clinical tasks like diagnosis, disease monitoring, and treatment planning by enabling precise identification, quantification, and tracking of anatomical and pathological features Fernandes et al. (2020). However, MRI segmentation, delineating anatomical structures or pathological regions from MRI scans, is labor-intensive, requires well-trained experts, and remains prone to inter-observer variability Joskowicz et al. (2019). These challenges arise from MRI’s variable tissue contrast (e.g., T1, T2, FLAIR, DWI), intensity inhomogeneity, protocols (Filippi and Agosta, 2007; Jager and Hornegger, 2009; Trattig et al., 2024), and the presence of small, clinically critical structures (Springer et al., 2016; Lee et al., 2024; Kraff et al., 2015; Harada et al., 2022; Haacke et al., 2020).

To reduce manual effort, traditional automated segmentation methods—such as atlas-based registration, statistical shape modeling, and intensity-driven clustering—were developed (Finnis et al., 2002; Nouranian et al., 2015; Dowling et al., 2015; Chandra et al., 2012). Atlas-based registration ensures anatomically consistent labels but is computationally expensive and results degrade with registration errors. Statistical shape models impose structural plausibility yet fail when pathological shapes

deviate from trained priors. Intensity-driven clustering methods are simple and training-free but are sensitive to MRI’s intensity nonuniformity and overlapping tissue contrasts. These limitations motivated the shift toward convolutional neural networks (CNNs) Chua (1997), which learn hierarchical representations directly from data to achieve more accurate and generalizable segmentation.

Early automated segmentation approaches relied on explicit anatomical priors Cabezas et al. (2011) and low-level image intensity Despotović I (2015) information to reduce manual effort, while modern CNN-based methods have substantially improved segmentation accuracy by learning hierarchical representations directly from data. Despite their success, CNN-based models typically require task-specific training and retraining when segmentation targets change, limiting scalability and generalization across scanners, contrasts, and anatomical regions (Renard et al., 2020; Ren et al., 2024; Stringer et al., 2021; Salehi et al., 2023). These constraints pose practical challenges in real clinical environments, where new targets and imaging protocols frequently emerge.

Recent advances in transformer-based architectures aim to overcome CNNs’ limited generalization and task-specific retraining requirements by learning more transferable and prompt-driven representations Yao et al. (2024). In particular, the Segment Anything Model (SAM) introduces a prompt-driven segmentation paradigm that enables zero-shot and interactive segmentation without task-specific retraining. Kirillov et al. (2023).

*Corresponding author.

Email address: zhao.wang1@uq.edu.au (Zhao Wang)

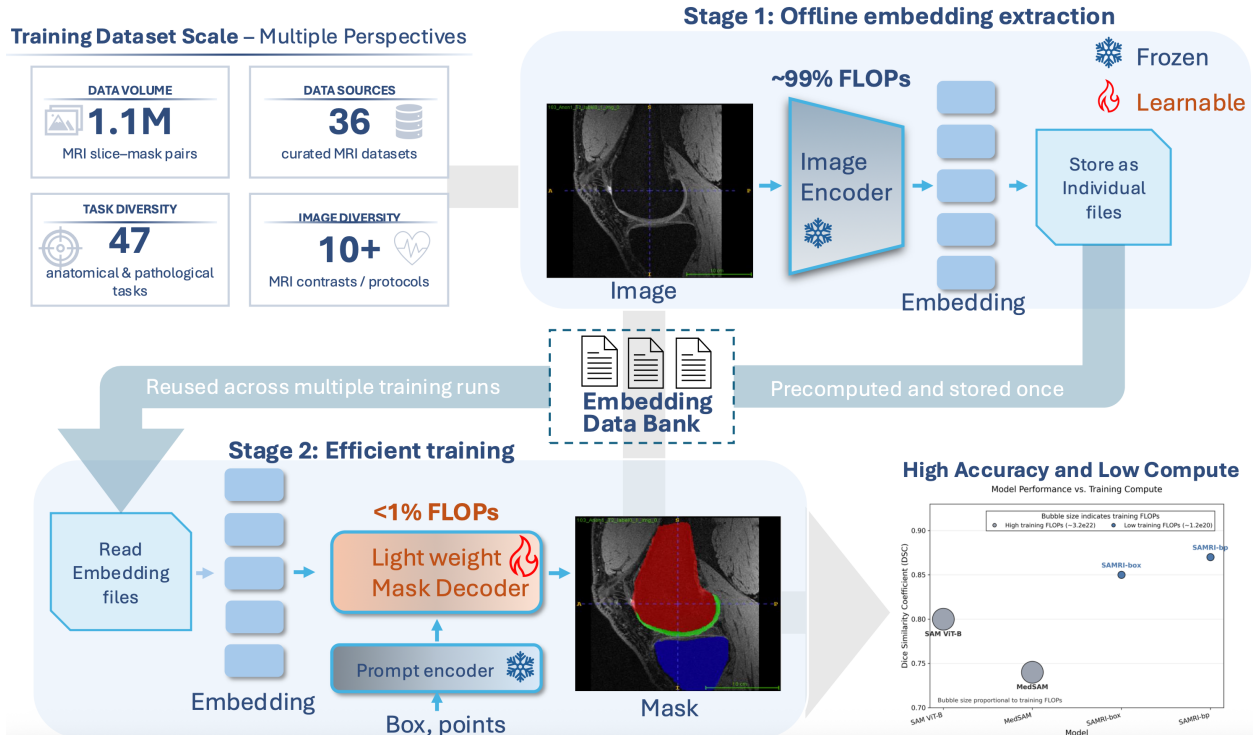


Figure 1: The SAMRI training framework. A large-scale MRI dataset (1.1 M slice-mask pairs from 36 datasets, 47 tasks, and 10+ contrasts) is used with a two-stage strategy—**Stage 1**: one-time offline embedding extraction with a frozen image encoder, and **Stage 2**: efficient training that reuses stored embeddings to optimize only a lightweight mask decoder with prompt inputs, achieving high accuracy with substantially reduced computational cost compared to full-model training.

SAM’s prompt-based design—accepting user-provided points, bounding boxes, or textual cues as segmentation prompts—enables zero-shot segmentation and interactive refinement without retraining, reducing annotation effort and offering flexibility for diverse targets Kirillov et al. (2023). While SAM demonstrates strong generalization on natural images, its direct application to MRI remains challenging due to fundamental differences between natural and medical imaging domains (Li et al., 2024; Mazurowski et al., 2023; Huang et al., 2024; Sack, 2023). Several studies (Ma et al., 2024; Dong et al., 2024; Gao et al., 2024) have adapted SAM for medical image segmentation through strategies such as full-model fine-tuning, parameter-efficient adaptation, and prompt refinement. Although these approaches highlight the potential of promptable segmentation in clinical workflows, yet they are often limited by insufficient MRI coverage, inadequate performance on small but clinically significant structures, and/or substantial computational overhead during model training (Ma et al., 2024; Wu et al., 2025; Nouman et al., 2024).

To address these gaps, we present SAMRI, an MRI-specialized adaptation of SAM that improves segmentation accuracy, particularly for small, clinically significant structures, while achieving training efficiency through a two-stage strategy tailored to MRI data (Fig. 1). Specifically, SAMRI first pre-computes image embeddings, compact latent representations generated from MRI slices using SAM’s pretrained image encoder, and then update only the mask decoder, while keeping the prompt encoders frozen. This design substantially reduces train-

ing cost and hardware requirements while retaining the strong feature extraction capability. SAMRI is trained on a curated, large-scale MRI corpus encompassing 47 tasks, over 10 MRI contrasts, and 1.1 million slice-mask pairs spanning whole-body organs and pathologies. As a result, SAMRI demonstrates robust cross-contrasts segmentation performance and strong zero-shot generalization, meaning it can segment previously unseen structures or imaging modalities without additional training. Our main contributions are:

(i) Improved performance on small-to-medium objects that are both common and clinically important in MR images. Owing to SAMRI’s large-scale and diverse training corpus—covering a naturally imbalanced distribution of object sizes—the model learns to effectively handle the small and medium structures that dominate MRI data. Consequently, SAMRI attains mean Dice 0.84 (small) and 0.85 (medium) versus MedSAM 0.59 and 0.67, yielding gains of up to 42.4% and 26.9% respectively.

(ii) A lightweight two-stage training procedure that freezes SAM’s encoders and trains only the mask decoder with a combined focal-Dice loss, reducing practical training time by 94% and trainable parameters by 96%, and training FLOPs by approximately 99% compared with full-model retraining, thereby making feasible even on a single commercial GPU.

(iii) State-of-the-art overall accuracy and zero-shot performance, achieving a mean Dice of 0.87 across 47 targets and 0.85 in zero-shot evaluation, surpassing MedSAM (0.74) by 17.6%, demonstrating SAMRI’s strong generalization across unseen MRI anatomies and imaging contrasts.

(iv) Practical deployment, providing a complete training-to-inference pipeline and a user-friendly local Graphical User Interface (GUI) for interactive application of pretrained SAMRI models on standard machines.

2. Background

Automated medical image segmentation has evolved substantially over recent years, progressing from model-driven approaches to data-driven learning paradigms and, more recently, foundation models pretrained on large-scale datasets. This section reviews major methodological developments relevant to MRI segmentation, including classical model-driven methods, CNN-based architectures, and prompt-driven foundation models. We further discuss the limitations of existing approaches in terms of generalization, training efficiency, and performance on small anatomical structures, which collectively motivate the development of SAMRI.

2.1. Model-driven and CNN-based Segmentation Methods

Early methods, including atlas-based registration, statistical shape modeling, and intensity-driven clustering, leveraged anatomical priors or voxel-level intensity statistics to generate segmentations Finnis et al. (2002). Atlas-based registration ensures anatomically consistent labels but is computationally expensive and results degrade with registration errors Nouranian et al. (2015). Statistical shape models impose structural plausibility yet fail when pathological shapes deviate from trained priors Dowling et al. (2015). Intensity-driven clustering methods are simple and training-free but are sensitive to MRI’s intensity nonuniformity and overlapping tissue contrasts Chandra et al. (2012). These limitations led to the adoption of CNNs, which learn hierarchical representations directly from data to achieve more accurate and generalizable segmentation. Convolutional neural networks have since become the dominant paradigm in medical image segmentation due to their hierarchical feature extraction and robust representational power Azad et al. (2024). Representative architectures such as U-Net and its numerous variants (e.g., VNet, 3D U-Net, Attention U-Net, nnU-Net)—along with other CNN-based designs like CAN3D—have achieved state-of-the-art performance in both 2D and volumetric segmentation (Çiçek et al., 2016; Zhu et al.; Harirpoush et al., 2024; Oktay et al., 2018; Dai et al., 2022; Zhang et al., 2023; Isensee et al., 2018; Alom et al., 2019; Milletari et al.; Ronneberger et al., 2015). However, CNN-based models still suffer from limited generalization across contrasts and scanners, weak segmentation capability for unseen targets, and the need for complete retraining when label sets change, constraining their scalability in dynamic clinical environments (Stringer et al., 2021; Kushol et al., 2023; Nomura et al., 2024; Renard et al., 2020; Ren et al., 2024). These limitations have motivated interest in foundation models that aim to learn more transferable representations across tasks and domains.

2.2. Foundation Models for Segmentation: SAM

Foundation models pretrained on large-scale datasets have recently attracted attention in image segmentation due to their

potential to improve generalization and reduce task-specific retraining Noh S (2025). The Segment Anything Model, pretrained on 11 million natural images with 1.1 billion masks, represents a prominent example, introducing a prompt-driven segmentation framework that supports zero-shot inference and interactive refinement using user-provided cues such as points or bounding boxes. The vanilla SAM architecture consists of three main components: an image encoder, a prompt encoder, and a mask decoder. The image encoder is based on a Vision Transformer (ViT-B/16 variant in our implementation) that processes RGB images by dividing them into 16×16 patches and passing them through 12 transformer layers to produce a 64×64 feature map. This encoder captures both local and global context across the image and was pretrained using a masked autoencoder He et al. (2022) strategy. The prompt encoder converts user-provided inputs, such as points or bounding boxes, into 256-dimensional embeddings that guide the segmentation process. These embeddings are combined with image features in the mask decoder, which is designed for efficiency and interactivity. The decoder consists of two transformer layers and a small convolutional head, producing a low-resolution mask (256×256) that is subsequently up-sampled to the original image size.

Despite its robust generalization on natural images, SAM is not specifically designed for medical images, particularly MRI, and consequently exhibits limitations arising from fundamental domain differences (Li et al., 2024; Mazurowski et al., 2023; Huang et al., 2024). MRI is characterized by subtle tissue boundaries, small or irregularly shaped structures, and pronounced foreground-background class imbalance, where only a small fraction of pixels correspond to clinically relevant targets Sack (2023). In contrast, SAM’s pretraining data predominantly contains larger objects Kirillov et al. (2023), which limits its ability to accurately segment small, clinically significant targets in MRI. These discrepancies often result in degraded performance when SAM is applied directly to MRI data.

2.3. SAM Adaptation Strategies for Medical Image Segmentation

To mitigate the domain gap between natural and medical images when applying SAM, several adaptation strategies have been proposed, which can be broadly grouped into three categories (See Table 1).

Full fine-tuning approaches, such as MedSAM Ma et al. (2024), update all SAM parameters using medical datasets. While this strategy can achieve robust performance across multiple medical modalities (e.g., CT, fundus, X-ray, and ultrasound), it often yields inconsistent results on MRI due to domain gaps among medical modalities (Nouman et al., 2024; Zhao et al., 2025; Deng et al., 2024; Wong et al., 2024). Moreover, full-model fine-tuning is computationally demanding and frequently infeasible for most research or clinical environments, limiting its scalability in practice.

Adapter-based methods, including Med-SA and MA-SAM (Chen et al., 2024; Wu et al., 2025), introduce lightweight trainable adapter layers while keeping SAM’s core weights frozen. EMedSAM Dong et al. (2024) further distills SAM’s image encoder into a lightweight student encoder, while reusing the

Table 1: Model comparison overview.

Model	Training scope	Methods	MRI data	Limitations
MedSAM	1.5M medical images across modalities, including MRI, CT, endoscopy, ultrasound, X-ray, pathology, fundus, etc.	Fine-tune image encoder and mask decoder	Yes	High training cost; inconsistent MRI results.
Med-SA	BTCV (CT), REFUGE2 (optic RGB), BraTS2021 (MRI for brain), TNMIX (ultrasound), ISIC2019 (skin RGB).	Adapter encoder and decoder	Yes	Only validated on brain glioblastoma for MRI.
EMedSAM	FLARE2022 (CT), lung CT, X-ray, BraTS (MRI for brain).	Distillation on image encoder	Yes	Only validated on brain glioblastoma for MRI.
DeSAM	CHAOS (CT+MRI), NCI-ISBI (prostate MRI), I2CVB (prostate cancer MRI), PROMISE12 (prostate MRI).	Prompt enhanced on original SAM	Yes	Uses original SAM weights.
MedLSAM	16 CT datasets: GLIA, ACRIN, QPC-Radiomics, Head-Neck-PET-CT, HNSCC, autoPET, MELA, LIDC-IDRI, STOI2021, MSD-Lung, CBIS-DDSM, AMOS2022, Kits19, MSD-Colon, MSD-Pancreas, FLARE2022.	Prompt enhanced on original SAM	No	Uses original SAM weights.
SAM-Med2D	REFUGE2 (optic RGB), BraTS (MRI for brain), HAM10000 (skin RGB), SARTAJ, Br35H (MRI for brain), COVID19 radiography, LC25000.	Adapter encoder and decoder	Yes	MRI evaluation limited to brain tumor datasets.
MA-SAM	BTCV (CT), NCI-ISBI (prostate MRI), I2CVB (prostate cancer MRI), PROMISE12 (prostate MRI), EndoVis18 (robotic scene RGB), MSD-Pancreas (CT), MSD-Colon (CT), AMOS22 (CT+MRI).	Adapter for encoder; trained encoder and decoder; 3D	Yes	MRI evaluation limited to prostate datasets.
SAMRI (Ours)	36 MRI datasets covering 47 tasks and 1.1M image-mask pairs spanning whole-body organs and clinically relevant pathologies.	Fine-tune mask decoder only	Yes	-

References: MedSAM Ma et al. (2024); Med-SA Wu et al. (2025); EMedSAM Dong et al. (2024); DeSAM Gao et al. (2024); MedLSAM Lei et al. (2025); SAM-Med2D Sun et al. (2024); MA-SAM Chen et al. (2024).

Note: "MRI data" indicates whether MRI data were included in training or evaluation.

original prompt encoder and mask decoder. These designs substantially reduce the number of trainable parameters and training cost, enabling more efficient domain adaptation. However, their published weights are typically trained and validated on narrow anatomical or modality-specific datasets, limiting their applicability to diverse MRI contrasts and unseen anatomical regions. Moreover, although adapter training is computationally lightweight, the image embedding process remains the primary bottleneck during each training epoch, as these methods must repeatedly perform online feature extraction through the frozen SAM encoder—making overall training substantially slower than suggested by their reduced parameter count.

Prompt-enhancement methods, such as MedLSAM and DeSAM (Gao et al., 2024; Lei et al., 2025), retain SAM’s pre-trained weights but refine or enrich input prompts (e.g., through textual, geometric, or region-aware cues) to improve localization and boundary adherence. While these methods preserve SAM’s generalization, their reliance on original SAM’s pre-trained weights limits adaptation to MRI’s contrast heterogeneity and small-structure segmentation challenges.

A detailed comparison of existing SAM-based medical segmentation methods is provided in Table 1. Beyond model architecture, evaluation protocols—particularly object size definitions—play a critical role in assessing segmentation performance.

2.4. Object Size Bias in Natural and MRI Segmentation

Object size is a critical factor in segmentation performance analysis. In natural image benchmarks such as COCO, objects are categorized into small, medium, and large groups based on bounding-box area, with fixed thresholds (approximately 32×32 and 96×96 pixels) Pont-Tuset and Van Gool. This formulation has been widely adopted in foundation model evaluation,

including SAM, providing a standardized means of analyzing performance across object scales.

However, this bounding-box-based definition is ill-suited for MRI segmentation. MRI datasets contain a high proportion of small anatomical and pathological targets—such as microbleeds (2–5 mm), small metastases (<10 mm), thin cartilage (<3 mm), and early-stage lesions (3–5 mm) (Springer et al., 2016; Lee et al., 2024; Kraff et al., 2015; Harada et al., 2022; Haacke et al., 2020)—which may occupy only 10–100 pixels even in high-resolution scans. Many such targets are thin, elongated, or irregularly shaped, spanning a large bounding box while occupying only a small fraction of the image in true mask area. This mismatch motivates the adoption of MRI-aware object size definitions, which we introduce in Section 4.2.

3. Methods

Motivated by the limitations of existing SAM-based approaches for MRI segmentation, SAMRI adopts a two-stage training framework tailored to MRI data. In the following, we describe the two-stage training procedure, the large-scale MRI dataset construction and preprocessing pipeline, the sampling and data partitioning strategy, and the loss function used to optimize SAMRI.

3.1. SAMRI Two-Stage training procedure

SAMRI builds on SAM (ViT-B/16) by freezing the heavy-weight image encoder and training only the lightweight mask decoder. Reusing SAM’s pre-trained encoder—responsible for most of SAM’s computational cost during both training and inference (Supplementary Table S4)—allows us precompute embeddings once (Stage 1, Fig. 1) and fine-tune only the decoder

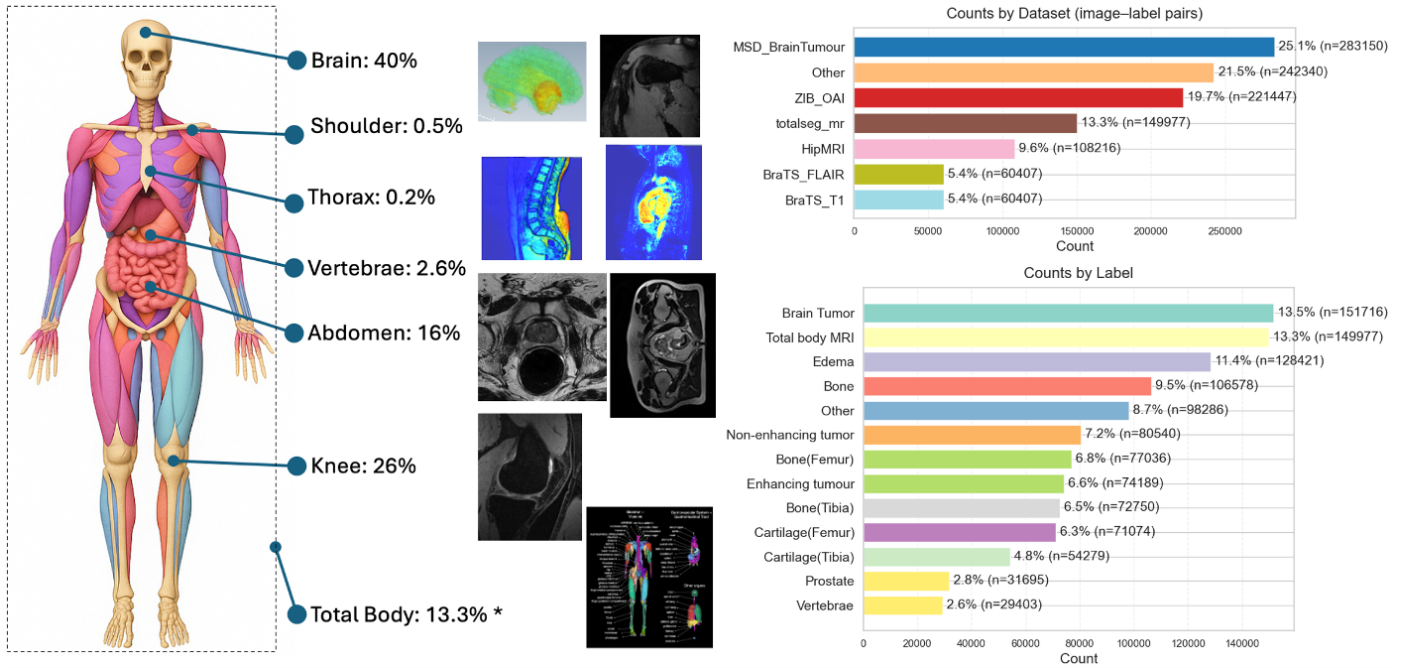


Figure 2: Composition of the SAMRI training corpus—anatomical coverage and dataset/task mix. **Left:** anatomical coverage of the 1.1 million MRI image-mask pairs used to train SAMRI, summarized by body region (Brain 40%, Knee 26%, Abdomen 16%, Vertebrae 2.6%, Shoulder 0.5%, Thorax 0.2%, and a Whole-body set 13.3%*). **Right:** distribution by **dataset** (top) and by **task/structure** (bottom). The corpus draws broadly from public MR datasets (e.g., MSD Brain Tumour, ZIB OAI, BraTS, HipMRI, and others), and spans a diverse set of targets including brain tumour subregions, whole-body organs, cartilage (femur/tibia), bone, edema, prostate, and vertebrae. This breadth across anatomies and sequences provides the variability needed for robust training and strong zero-shot generalization. * “Total Body” denotes whole-body, multi-organ MRI annotations from TotalSeg-MR for general purpose segmentation tasks.

for domain shift (Stage 2, Fig. 1), drastically reducing training cost. Empirically, in our setting, SAM ViT-H, the largest SAM variant, did not yield measurably better MRI segmentation than SAM ViT-B (Supplementary Fig. S9), suggesting that ViT-B features are already sufficient for MRI textures and contrasts; a similar observation was reported by others Huang et al. (2024). By concentrating learning in the decoder, SAMRI adapts specifically to MRI characteristics while preserving computational efficiency and improving segmentation accuracy. Removing the encoder from the online training loop eliminates redundant forward passes, yielding an approximate 88% reduction in total training time over 100 epochs (computational details are provided in Appendix A).

3.2. Dataset Collection and Preprocessing

Diversified Data Sources. We assembled 36 MRI datasets incorporating multi-organ/body region imaging spanning examinations of both healthy and pathological tissues: 21 inherited from MedSAM and 15 new MRI datasets added with additional tasks and contrasts. In the final corpus, about 72% of images come from the new datasets and 28% from MedSAM’s collection (Supplementary Fig. S1), broadening anatomical and contrast diversity and supporting stronger zero-shot generalization. Sources include Kaggle, OAI, TCIA, and MICCAI segmentation challenges. The collection covers 47 segmentation tasks across multiple MRI contrasts (T1, T2, FLAIR, DWI) and anatomical regions (brain, spine, knee, prostate, heart, abdomen). In total, we curated ~1.1 million expert-annotated 2D image-mask pairs.

A visual summary of the data sources is presented in Fig. 2, with a detailed breakdown provided in Table S1 in Supplementary.

Preprocessing Pipeline. The collected MRI data were in various formats (NIFTI, MATLAB, DICOM, NRRD, MetaImage Header) and included both 2D and 3D acquisitions. We standardized all data by:

- Converting all 3D MRI volumes into 2D slices in NIFTI format along the anatomical axis with the lowest dimension, ensuring each slice captures maximal structural details, and discarding all masks containing fewer than 10 labeled pixels. Such small masks typically occur near the edges of target structures or arise from annotation artifacts, introducing noise that can degrade model training.
- Performing patient-level splits (80%:10%:10% for train, validation, and test) to prevent data leakage.
- Discarding masks with fewer than 10% of the largest slice’s mask area, as such small masks typically arise from peripheral slices with incomplete anatomical coverage or annotation artifacts, which impair training stability.
- Normalizing grayscale MRI slices to [0, 255] integer range and replicating across three channels to match SAM’s RGB input requirements.

After pre-processing, the images were passed through the frozen SAM encoder to generate visual embeddings, which were computed once and stored on the Embedding Data Bank (Hard disk or data cluster) for reuse during decoder training (Fig. 1).

Sampling Strategy. To address dataset-level imbalance (ranging from 56 to 283K samples per dataset), we applied per-epoch resampling so that every dataset contributes a minimum of 5,000 samples. Specifically, small datasets are sampled with replacement until they reach this quota, while large datasets are subsampled without replacement—yielding a near-uniform dataset contribution per epoch. This raises the sampling probability of anatomies that occur primarily in small datasets, preventing gradient updates from being dominated by the largest corpora and thereby ensuring broader anatomical coverage during training.

Training and zero-shot datasets. We partitioned 36 MRI datasets into two groups (Supplementary Table S1): 30 datasets were used for the standard train, validation, and testing workflow; six were held out entirely for zero-shot evaluation. The 30-set pool was selected to maximize anatomical and contrast diversity (vendors, contrasts, resolutions), improving robustness and reducing overfitting. For the zero-shot benchmark, five datasets mirror MedSAM’s zero-shot suite to enable like-for-like comparison, while the sixth—MSK shoulder—was added to probe cross-anatomy transfer. Importantly, all six datasets are unseen for SAMRI, SAM, and MedSAM, ensuring a fair comparison. Because all training cartilage data are from the knee, performance on shoulder cartilage in MSK shoulder dataset assesses whether the model exploits structural similarity rather than anatomy-specific shortcuts. This design isolates generalization, prevents leakage between training and evaluation, and directly measures robustness to dataset and anatomical variations.

3.3. Loss Function

To train SAMRI effectively across diverse MRI segmentation tasks, we utilized a loss function that combines the strengths of both focal loss Lin et al. and Dice loss Sudre et al.. The final loss \mathcal{L}_{SAMRI} is defined as:

$$\mathcal{L}_{SAMRI} = 20 \cdot \mathcal{L}_{Focal} + \mathcal{L}_{Dice} \quad (1)$$

This formulation is particularly effective for small object segmentation, as focal loss prevents rare pixels (often corresponding to small structures) from being overwhelmed during training, while Dice loss ensures accurate boundary delineation, which is crucial when objects are present in sparse, low-pixel-count regions. \mathcal{L}_{Focal} and \mathcal{L}_{Dice} are defined in Appendix B.

4. Experiments

This section presents the experimental design used to evaluate SAMRI, including the training protocol, object size definition, baseline models, and statistical analysis. We focus on segmentation accuracy, computational efficiency, and robustness across diverse MRI targets under a unified evaluation setting.

4.1. Training protocol

The SAMRI model was initialized with the pre-trained SAM using the ViT-Base backbone. The prompt encoder was kept frozen, as it is already well-suited for processing bounding box

prompts. To simulate interactive segmentation, we generate synthetic box prompts from the ground truth segmentation masks by extracting the tightest bounding box around individual object in the image. To improve robustness and generalization, we apply random spatial shifts to the box coordinates by adding or subtracting up to 20 pixels during training. To retain its generalization capability in feature abstraction, the image encoder was also frozen during training. In contrast, the light-weight mask decoder was trained. This selective training strategy enables our efficient training procedure while maintaining SAM’s robust feature representations. Training was conducted using the AdamW optimizer Ren et al. (2024) with $\beta_1 = 0.9$, $\beta_2 = 0.999$, an initial learning rate of $1e-5$, and weight decay of 0.1. We used a global batch size of 1024 without data augmentation, given the scale and diversity of the 30 training datasets. Training was performed for 200 epochs on 8 AMD MI300X GPUs (each with 192 GB VRAM).

4.2. Object Size Definition and Stratification

As discussed in Section 2.4, COCO’s bounding-box-based size thresholds are ill-suited for MRI, where thin or elongated structures can span large bounding boxes while occupying minimal mask area. To address this, we define object size by mask area rather than bounding-box area, normalized by image resolution. Specifically, we bin samples by percentage of image area (mask pixels / image pixels), with cut-offs at 0.5% and 3.5% to form small, medium, and large categories (comparable to COCO’s cut-offs at 0.3% and 3%). Size bins are detailed in Table 4 and Fig. 4.

4.3. Baseline Models

We evaluate SAMRI against two representative SAM-based 2D models using DSC, HD, and MSD as evaluation metrics (details in Appendix C). SAMRI and SAM use identical pre/post-processing; MedSAM follows its published pipeline. All methods receive identical ground-truth-derived bounding-box prompts with no model-specific tuning.

- **SAM (ViT-B).** Official pretrained weights used in zero-shot evaluation, serving as the canonical foundation baseline without adaptation.
- **MedSAM.** A medical adaptation of SAM trained on ~1.5 million images across modalities (MRI, CT, ultrasound, X-ray), representing the current best general-purpose medical segmentation model based on SAM.

Inclusion criteria and rationale. We include only models with publicly available pretrained checkpoints suitable for MRI-wide, zero-shot evaluation. Within this scope:

- **ViT-H vs ViT-B.** On our development set, SAM ViT-H offered no consistent advantage over ViT-B in zero-shot MRI while being much heavier (Supplementary Fig. S9); we therefore adopt ViT-B as the canonical SAM baseline.
- **Adapter-based variants.** Most are trained primarily on CT or single-task MRI, or lack released foundation-scale checkpoints, preventing a fair MRI-wide comparison. (see Table 1)

Table 2: Summary segmentation performance across all 47 targets.

Model	DSC \uparrow	HD (px) \downarrow	MSD (px) \downarrow
SAM ViT-B	0.80 \pm 0.17	8.61 \pm 13.56	1.99 \pm 2.85
MedSAM	0.74 \pm 0.24	8.89 \pm 14.23	2.20 \pm 2.84
SAMRI_{box}	0.85 \pm 0.15	5.95 \pm 6.21	1.42 \pm 1.10
SAMRI_{bp}	0.87 \pm 0.11	5.36 \pm 4.07	1.30 \pm 0.76

DSC, HD, and MSD are reported as Mean \pm Standard Deviation across 47 anatomical and pathological targets. SAMRI_{box} denotes SAMRI with box-only prompts; SAMRI_{bp} denotes SAMRI with box+point prompts.

- **Prompt-enhanced methods.** These typically reuse the original SAM weights (e.g., DeSAM, MedLSAM in Table 1); differences largely reflect prompting heuristics rather than a distinct foundation model, so their intrinsic capacity aligns with the SAM baseline.

4.4. Statistical Analysis

Statistical significance was assessed using the Wilcoxon signed-rank test for paired comparisons between models across all 47 segmentation targets. This non-parametric test was chosen as the performance metrics were not normally distributed across diverse anatomical structures. We report p-values with $p < 0.05$ indicating significant differences.

5. Results

This section presents a comprehensive evaluation result of SAMRI in terms of segmentation accuracy, object size-stratified performance, training computational efficiency, and generalization. We first report overall quantitative results across 47 MRI targets and compare SAMRI with SAM ViT-B and MedSAM. We then analyze performance gains for small anatomical structures, provide qualitative visual comparisons, examine zero-shot generalization to unseen datasets, and assess training behavior and practical deployment considerations.

5.1. Segmentation Performance

We evaluated SAMRI—including box-only (SAMRI_{box}) and box+point (SAMRI_{bp}) prompt variants—against SAM ViT-B and MedSAM (Table 2). Across 47 anatomical and pathological targets from 36 datasets, SAMRI_{bp} achieved the best overall performance, with the highest mean DSC (0.87 \pm 0.11) and lowest boundary errors (HD: 5.36 \pm 4.07 px; MSD: 1.30 \pm 0.76 px). SAMRI_{box} also performed well (DSC: 0.85 \pm 0.15; HD: 5.95 \pm 6.21 px; MSD: 1.42 \pm 1.10 px), with SAMRI_{bp} showing modest but consistent advantages across most targets. Both SAMRI variants significantly outperformed MedSAM and SAM ViT-B across all metrics (Wilcoxon signed-rank test, $p < 0.05$). Full per-target and per-dataset results are provided in Supplementary Tables S2–S3 and Figs. S2–S8.

During training, VRAM usage can be reduced by lowering the batch size, with a practical minimum of \sim 2.5 GB. Precomputed image embeddings required \sim 2.2 TB of storage (\sim 1.1 million image-mask pairs), and the final checkpoint is \sim 350 MB. Practically, SAMRI_{bp} can be trained on a single commercial GPU

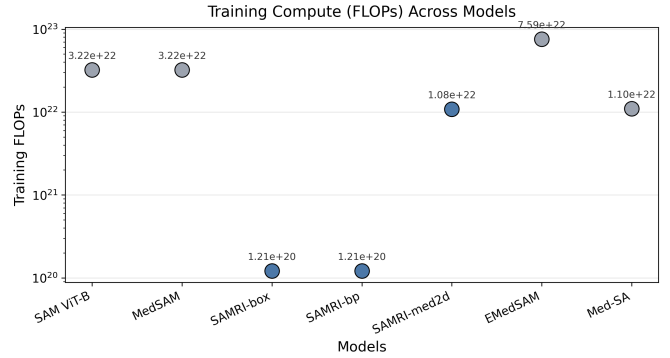


Figure 3: Training FLOPs across models. Total training floating-point operations (FLOPs) required by each model, shown on a logarithmic scale. SAM ViT-B and MedSAM require 3.22×10^{22} FLOPs. Adapter- or end-to-end-trained variants incur higher computational costs, including SAMRI-med2d (1.08×10^{22}), EMedSAM (7.59×10^{22}), and Med-SA (1.10×10^{22}) FLOPs. In contrast, SAMRI-box and SAMRI-bp require only 1.21×10^{20} FLOPs, corresponding to an approximate 99% reduction in training compute relative to SAM ViT-B and MedSAM. FLOPs are calculated based on training for 200 epochs on 1.1 M slice-mask pairs using a Mac mini (M4) chip.

Table 3: Experimental results on commercial devices

Metric	Image \rightarrow Embedding (Precomputing)	Image \rightarrow Mask (Inference)	Train from Embedding (Embedding Once)	Train from Image (Embedding Every Epoch)
Time	50.43 s	55.09 s	4.42 s / epoch	63.23 s / epoch
Memory usage	4.40 GB	4.46 GB	2.28 GB	6.73 GB

Note: Results are based on 100 2D NIfTI-format MR image-mask pairs. Test device: Apple Mac mini M4 Pro, 24 GB unified memory.

in around one month on million-sample datasets, indicating that the two-stage procedure enables feasible fine-tuning of a state-of-the-art model. See Table 3 for detailed experiments on a Mac mini.

5.2. Substantial Gains in Small-Object Segmentation

Across all size bins, SAMRI (box and box+point) outperforms both SAM ViT-B and MedSAM (Table 4). For small structures ($< 0.5\%$ of image area), SAMRI_{bp} reaches 0.84 ± 0.26 DSC—an absolute gain of $+0.25$ over MedSAM ($+42.4\%$), with SAMRI_{box} similar at 0.83 ± 0.31 . For medium-sized targets ($0.5\text{--}3.5\%$ of image area), SAMRI_{bp} attains 0.85 ± 0.22 , improving on MedSAM by $+0.18$ ($+26.9\%$). Even for large objects ($> 3.5\%$), where baselines are already strong, SAMRI_{bp} maintains a measurable edge (0.95 ± 0.12 vs 0.92 ± 0.16 ; $+0.03$, $+3.3\%$). Overall, the largest relative gains appear in the small and medium regimes, consistent with SAMRI’s design emphasis on challenging clinically important small structures.

Fig. 4 further illustrates the relationship between segmentation performance and object size. The top left panel shows the

Table 4: DSC performance by object size category.

Size Category*	Object Area*	SAM ViT-B	MedSAM	SAMRI _{box}	SAMRI _{bp}	Δ vs MedSAM†
Small	$< 0.5\%$ of image	0.76 \pm 0.34	0.59 \pm 0.47	0.83 \pm 0.31	0.84 \pm 0.26	$+0.25$ ($+42.4\%$)
Medium	$0.5\text{--}3.5\%$ of image	0.77 \pm 0.34	0.67 \pm 0.42	0.85 \pm 0.26	0.85 \pm 0.22	$+0.18$ ($+26.9\%$)
Large	$> 3.5\%$ of image	0.91 \pm 0.18	0.92 \pm 0.16	0.95 \pm 0.13	0.95 \pm 0.12	$+0.03$ ($+3.3\%$)

DSC: Dice similarity coefficient.

*Size bins stratified by object area (percentage of image) using the global distribution.

† Δ and % computed for SAMRI_{bp} relative to MedSAM ($\Delta = \text{SAMRI}_{bp} - \text{MedSAM}$; % = Δ / MedSAM).

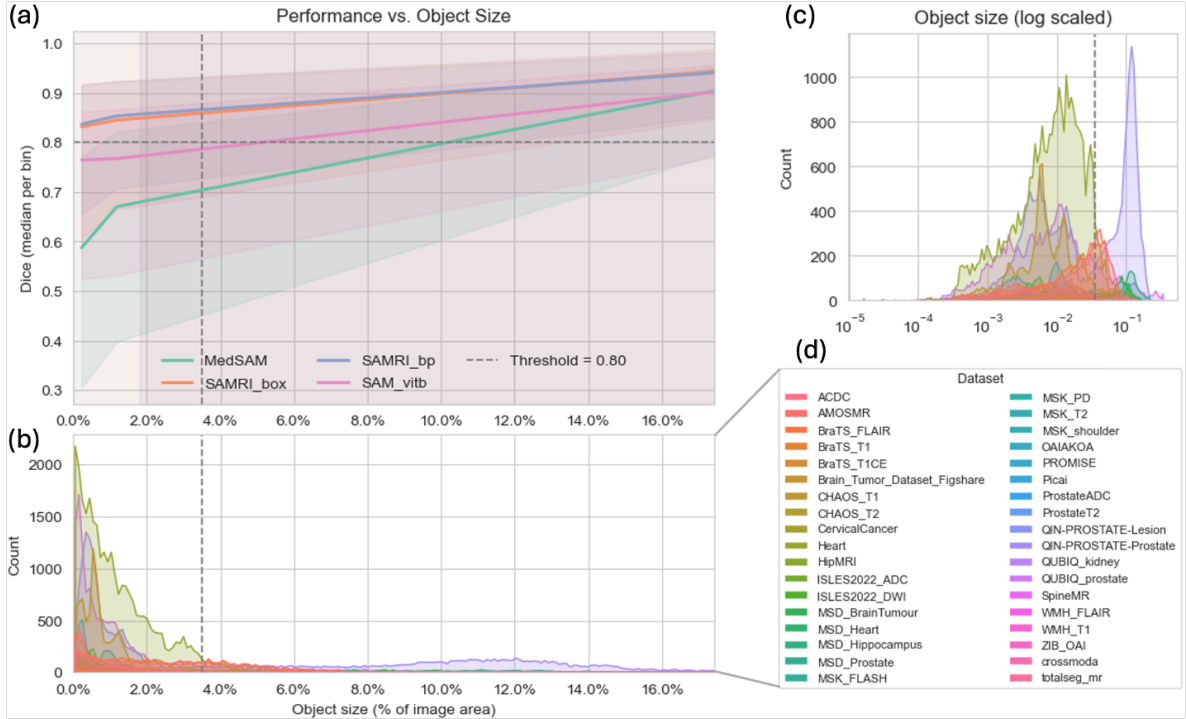


Figure 4: Performance vs. object size. (a) Median Dice (\pm IQR) by object-size bin; the horizontal dashed line marks the 0.80 as a heuristic baseline. The vertical dashed line separates large objects ($>3.5\%$ of image area) from small/medium ($<3.5\%$). SAMRI attains the highest Dice across sizes, with the largest gains in the small-medium regime. (b) Histogram of training samples by object size (same x-axis), showing a dominance of small objects. (c) Log-scaled object-size distribution for the full dataset, again indicating small-object dominance. (d) Legend for the 36 datasets.

median DSC (\pm IQR: Interquartile Range) across size bins. We include a dashed reference at DSC = 0.80 as a heuristic baseline. SAMRI consistently stays above this threshold and demonstrates the most significant gains for small and medium objects, where competing methods show a steep drop in accuracy.

The bottom panel presents the distribution of object sizes in the dataset, showing that the vast majority of training samples are small structures ($<3.5\%$ of image area). This highlights the practical importance of SAMRI’s improvement in this regime, as small anatomical targets are both abundant in MRI data and often critical for clinical decision-making.

Notable improvements were observed in several small anatomical structures (Supplementary Table S2). For example, SAMRI achieved a DSC of 0.85 on femoral cartilage, whereas MedSAM struggled (0.00 DSC). In the extra-meatal part of a vestibular schwannoma, SAMRI reached 0.84 DSC compared to 0.57 for MedSAM, which corresponds to a 45% improvement. The left adrenal gland showed 0.85 DSC versus 0.63 (a 35% gain), and the cochlea achieved 0.86 DSC versus 0.73 (an 18% gain). These results highlight the substantial advantage of SAMRI in segmenting small, clinically significant MRI structures—domains where baseline models fail or underperform.

5.3. Qualitative Analysis

Fig. 5 presents qualitative comparisons across diverse anatomies and MRI contrasts. SAMRI consistently produces smoother and more anatomically coherent contours than MedSAM and SAM ViT-B. Specifically, baseline models exhibit two

common failure modes: (1) *boundary over-extension*, where predicted contours extend beyond the true structure into adjacent tissue (e.g., Row 2 left, kidney: MedSAM’s magenta contour extends into surrounding tissue; Row 3 middle, prostate: SAM ViT-B significantly over-segments the target region), and (2) *missed fine structures*, where thin or low-contrast regions are incompletely segmented (e.g., Row 1 left and middle, brain tumor: baseline models fail to capture the irregular tumor boundaries; Row 4, femur cartilage: SAM ViT-B and MedSAM miss portions of the thin cartilage structure). In contrast, SAMRI variants maintain precise boundary delineation even in these challenging regions. When structures have clear, well-defined boundaries, all models perform comparably well. For example, in Row 2 middle (left atrium) and Row 2 right (prostate), all four methods achieve similar segmentation quality, with contours closely aligned to the ground truth.

The difference between SAMRI_{box} and SAMRI_{bp} remains modest overall; however, the additional point prompt in SAMRI_{bp} provides consistent refinement around ambiguous borders (e.g., Row 3 left and right, prostate: the green contour shows tighter adherence to ground truth than the orange contour). These visual patterns align with the quantitative results in Table 4: the most pronounced improvements occur on small and medium structures with ambiguous boundaries, while performance on large, well-defined objects remains comparable across methods.

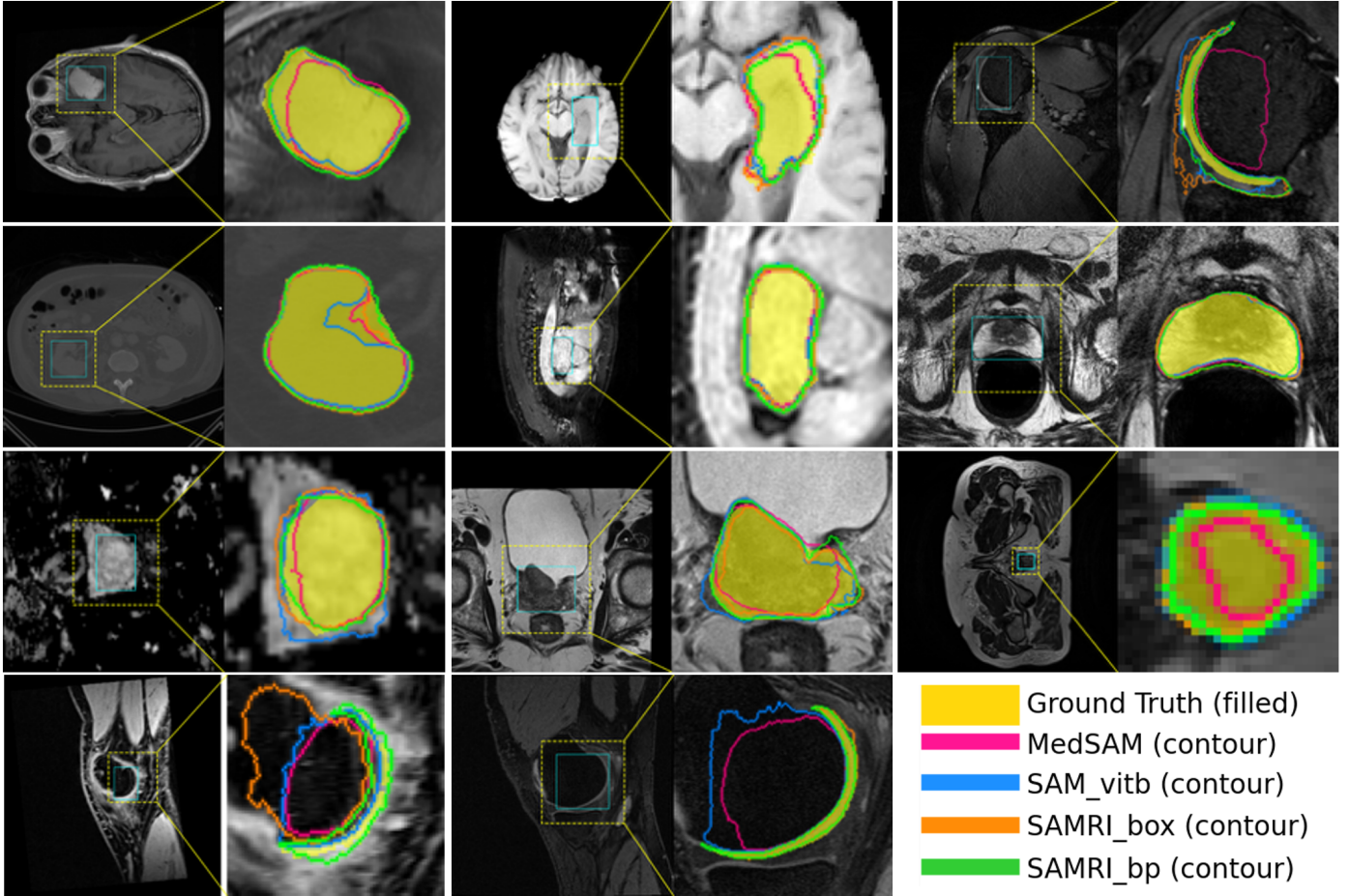


Figure 5: Qualitative comparisons across anatomies and contrasts. Each case shows the full image with a zoom-in. Ground truth (yellow fill); SAM ViT-B (blue), MedSAM (magenta), SAMRI_{box} (orange), SAMRI_{bp} (green) contours. SAMRI variants adhere more closely to the reference, especially on thin or small structures and low-contrast regions; SAMRI_{bp} most consistently captures fine extremities and concavities.

5.4. Zero-shot Generalization

We evaluated SAMRI’s zero-shot generalization on six unseen datasets (Fig. 6). SAMRI_{bp} achieved consistently strong performance across datasets, while MedSAM and SAM ViT-B exhibited larger variability or lower median Dice scores. The size-stratified view (right) pinpoints the source of these gains: for small and medium targets, the SAMRI distributions shift upward with higher medians and substantially higher lower quartiles, while performance on large objects remains competitive. Notably, the MSK shoulder dataset includes humerus and scapula cartilage whose properties resemble knee cartilage (see Fig 5: upper-right: shoulder cartilage; bottom row: knee cartilage); training on knee cartilage appears to transfer effectively to these anatomically distinct yet structurally similar targets, boosting zero-shot performance. Beyond overall accuracy, SAMRI also exhibits narrower IQR and fewer catastrophic outliers, indicating improved robustness to contrast, noise, and label conventions. Overall, SAMRI lifts the zero-shot accuracy without sacrificing stability, with the box+point prompt yielding the most reliable improvements.

5.5. Training and validation loss observation

Across both box-only and box+point prompting, training loss decreases smoothly while seen-set validation loss remains largely flat, indicating no overfitting (Fig. 7). We monitor two criteria: (i) zero-shot validation loss on a held-out 10% ACDC split and (ii) seen-set validation loss. The minimum zero-shot loss occurs at epoch 40 for both prompting regimes, whereas the seen-task minima occur later—epoch 150 for box-only and epoch 170 for box+point. To accommodate different deployment needs, we therefore retain four checkpoints: box-only @ 40 (simplest prompt; best zero-shot accuracy, i.e., lowest zero-shot loss), box-only @ 150 (simplest prompt; best seen-task accuracy), box+point @ 40 (highest zero-shot accuracy), and box+point @ 170 (highest seen-task accuracy).

5.6. Practical deployment and interactive segmentation

We further demonstrate the practical usability of SAMRI through a user-friendly local graphical interface (Supplementary Fig. S11). The interface supports interactive visualization of volumetric MR images and prompt-based segmentation using bounding boxes and point prompts, with segmentation results displayed in real time for iterative refinement. Pretrained

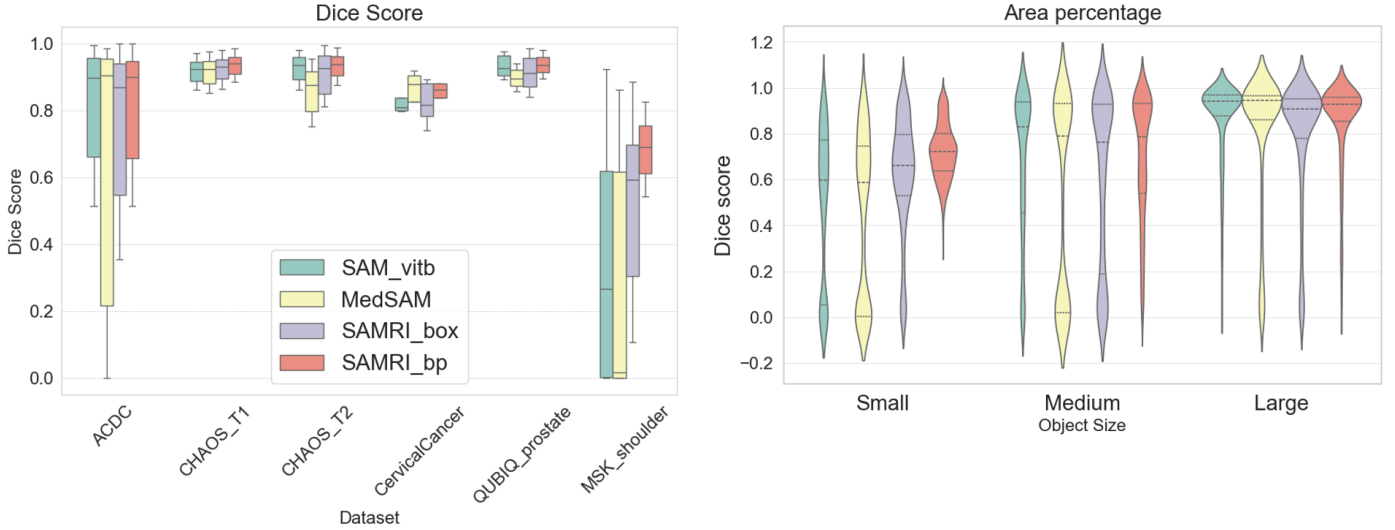


Figure 6: Zero-Shot Performance Across Datasets and Object Sizes. (a) Dataset-wise Dice boxplots on held-out (zero-shot) sets. SAMRI_{bp} achieved consistently strong performance across datasets, with SAMRI_{box} performing comparably, while MedSAM and SAM ViT-B exhibited larger variability and lower median Dice scores in some datasets. (b) Size-stratified violin plots (small/medium/large). SAMRI variants shift the distributions upward for small and medium targets (higher medians and lower tails) while remaining competitive on large objects.

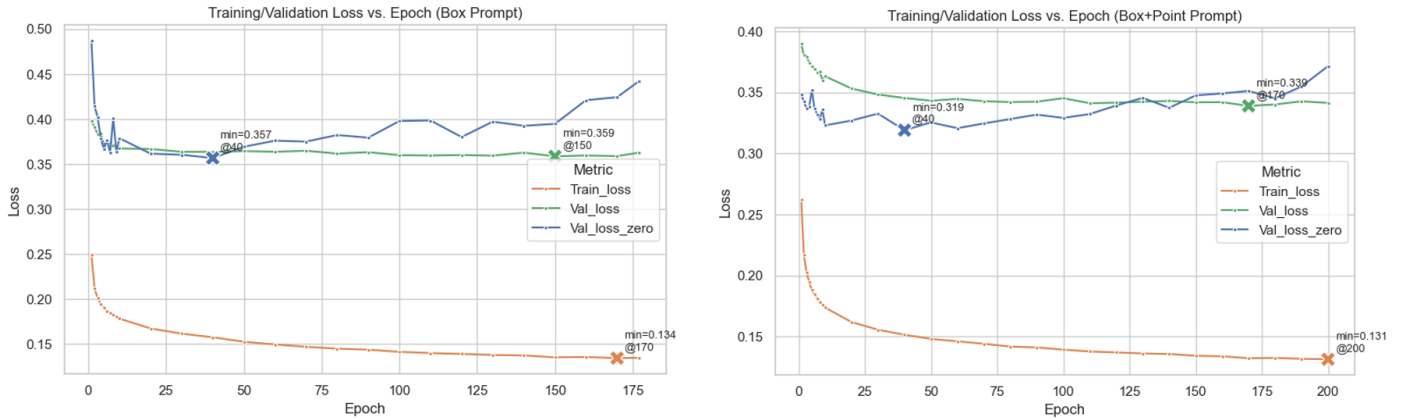


Figure 7: Loss trajectories across epochs. Left: box prompt; right: box+point prompt. Plotted are training loss (orange), seen-set validation loss (green), and zero-shot validation loss (blue). The curves indicate stable convergence without overfitting on seen datasets, with optimal zero-shot performance at around epoch 40.

SAMRI models can be applied directly on standard local machines without specialized deployment infrastructure, enabling efficient and responsive interaction, typically within seconds per slice on a single commercial GPU with >4.5 GB VRAM. By abstracting preprocessing, model loading, and inference, the interface lowers the technical barrier for end users and facilitates practical adoption of SAMRI for interactive MRI segmentation.

6. Discussion

This work introduces SAMRI, an MRI-specialized adaptation of SAM that updates only the mask decoder on pre-computed image embeddings, enabling an efficient training pipeline. Across 47 anatomical/pathological targets and 36 datasets, SAMRI—especially the box+point variant—outperforms SAM ViT-B and MedSAM in Dice and boundary metrics, with the largest gains on small and medium structures. Qualitative anal-

yses show reduced over-segmentation into adjacent tissue and more precise boundary adherence on thin or low-contrast targets, aligning with the size-stratified improvements. SAMRI also attains strong zero-shot performance on six held-out datasets, indicating robust generalization.

Why it works. We attribute the gains to the following factors: (i) retaining SAM’s pretrained image encoder while updating only the mask decoder allows MRI-specific adaptation without losing general visual representations; (ii) a two-stage pipeline (Fig. 1) that precomputes image embeddings and then trains the decoder avoids redundant encoder passes, substantially reducing computational cost and memory usage; (iii) training on a broad, MRI-only corpus spanning different contrasts and anatomies regularizes the decoder toward MRI-specific textures, rather than features from other modalities (e.g., CT/X-ray/ultrasound) that may not generalize to MRI. Finally, the box+point prompt enhances spatial guidance: the box provides

coarse localization, while the point specifies the intended target, reducing ambiguity in small, or low-contrast regions.

Small objects matter. Most samples in our corpus occupy <3.5% of the image area. In that regime, baselines drop sharply in accuracy, whereas SAMRI raises the entire curve above the 0.80 threshold. These targets—cartilage, small lesions, vessels—are common and clinically important in MRI, often driving clinical decisions. SAMRI better preserves narrow tips and concavities while avoiding over-segmentation into adjacent tissue, as reflected in both quantitative margins and visual comparisons. Training on an MRI-only corpus avoids modality-specific artifacts and sharpens the decoder’s inductive bias for MRI textures, explaining why SAMRI gains most where baseline priors are weakest on small, low-contrast targets.

Efficiency and practicality. Training completes in ~76 hours on 8× MI300X (~608 GPU-hours), and inference requires only ~4.5 GB of VRAM. This represents a substantial improvement over full-model retraining and adapter-based methods that recompute image features every epoch, making SAMRI practical for typical academic and clinical compute environments.

Zero-shot generalization. On unseen datasets, SAMRI maintains higher median Dice scores and smaller variance than comparators. Gains are largest for small and medium objects, while performance on large structures remains competitive evidencing that decoder specialization enhances adaptation to MRI statistics without compromising generalization across scanners, contrasts, or labeling conventions. This robustness is crucial for deployment in heterogeneous clinical settings where retraining is costly or impractical. Notably, training solely on knee cartilage substantially improves zero-shot performance on shoulder cartilage, indicating that exposure to diverse yet structurally related examples enhances transfer. More broadly, these results support our choice to train on a large, MRI-only corpus spanning sequences and anatomies, rather than narrow, modality-specific subsets (as in many adapter-based baselines in Table 1), to maximize zero-shot generalization.

Limitations. First, our pipeline supports 2D slices currently, foregoing inter-plane context that can help disambiguate boundaries. Second, despite broad coverage, dataset composition may still under-represent certain vendors, rare pathologies, or pediatric populations; residual domain shift is possible. Third, label noise and inter-rater variability—ubiquitous in public MRI sets—can cap achievable metrics and may differentially affect small-object evaluations (Supplementary Fig. S10). Fourth, while embedding precomputation accelerates training, it requires ~2.2 TB of storage at full scale; clinics with constrained storage may need cloud or streamed variants. Finally, we did not study uncertainty calibration or failure detection, both critical for safe clinical use.

Future work. Extending SAMRI to 2.5D or 3D architectures with explicit inter-slice context may further improve robustness, particularly for thin structures and regions with ambiguous boundaries. On the data side, we plan to expand pretraining and fine-tuning to broader, multi-institutional MRI cohorts to enhance out-of-domain generalization. While a graphical user interface is already provided, the current implementation is based on a Jupyter notebook environment and may offer lower runtime

efficiency than standalone desktop applications; future work will focus on developing a system-level and web-server-based interface to further improve usability and deployment flexibility.

Conclusion

SAMRI is an MRI-specialized adaptation of SAM that fine-tunes only the mask decoder on precomputed embeddings, trained on a large, multi-sequence MRI resource spanning whole-body organs and clinically relevant pathologies. It achieves state-of-the-art accuracy, especially for small, clinically salient structures, while remaining computationally frugal and deployment-ready. The combination of strong zero-shot generalization, training efficiency, and practical VRAM requirements makes SAMRI a viable foundation for MRI segmentation in real-world settings. Importantly, SAMRI could materially aid clinical researchers by enabling semi-automatic annotation, streamlining workflows that require manual corrections, and improving robustness for models intended for clinical use—especially in data-scarce settings such as rare diseases.

Declaration of generative AI and AI-assisted technologies

During the preparation of this work the author(s) used ChatGPT in order to check grammar and refine language. After using this tool/service, the author(s) reviewed and edited the content as needed and take(s) full responsibility for the content of the published article.

Appendix A. Efficiency gain

Without precomputing embeddings, the wall-clock training time over N epochs is

$$T_{\text{total}} = N \times (T_{\text{data}} + T_{\text{enc}} + T_{\text{dec}} + T_{\text{bp}}), \quad (\text{A.1})$$

where T_{total} denotes the total training time, T_{data} is the data loading and preprocessing time, T_{enc} is the image encoder inference time, T_{dec} is the mask decoder inference time, and T_{bp} is the backpropagation time.

With our two-stage pipeline (one-time embedding computation followed by decoder-only training), the total training time becomes

$$T_{\text{pipeline}} = T_{\text{data}} + T_{\text{enc}} + N \times (T_{\text{dec}} + T_{\text{bp}}). \quad (\text{A.2})$$

By removing the encoder from the per-epoch training loop, the pipeline avoids $(N - 1)T_{\text{enc}}$ redundant computations. In our experimental setting ($N = 100$ epochs), eliminating these 99 encoder forward passes results in an approximately 88% reduction in wall-clock training time.

Appendix B. Focal loss and Dice loss

Let S and G represent the predicted segmentation and ground truth mask, respectively, and let s_i, g_i denote the predicted and true values at pixel i across all N pixels in an image. The focal loss (\mathcal{L}_{Focal}) is defined as equation (A.1):

$$\mathcal{L}_{Focal} = -\frac{1}{N} \sum_{i=1}^N \alpha (1 - p_i)^\gamma \log(p_i) \quad (\text{B.1})$$

Where:

- $p_i = s_i$ if $g_i = 1$, otherwise $p_i = 1 - s_i$
- $\alpha \in [0, 1]$: weighting factor for balancing positive vs. negative samples (optional)
- $\gamma > 0$: focusing parameter that reduces the relative loss for well-classified examples
- $\log(p_i)$: standard cross-entropy term

The Dice loss \mathcal{L}_{Dice} is defined as equation (A.2):

$$\mathcal{L}_{Dice} = 1 - \frac{2 \sum_{i=1}^N s_i g_i}{\sum_{i=1}^N (s_i)^2 + \sum_{i=1}^N (g_i)^2} \quad (\text{B.2})$$

Appendix C. Evaluation metrics

We evaluate model performance using three complementary metrics that capture both region overlap and boundary accuracy:

Dice Similarity Coefficient (DSC) Dice (1945): Measures region overlap between predicted segmentation S and ground truth G :

$$\text{DSC}(S, G) = \frac{2 \sum_{i=1}^N s_i g_i}{\sum_{i=1}^N s_i + \sum_{i=1}^N g_i} \quad (\text{C.1})$$

Where:

- N : total number of pixels in the image.
- $s_i \in \{0, 1\}$: predicted value for the i -th pixel (1 for foreground, 0 for background).
- $g_i \in \{0, 1\}$: ground truth label for the i -th pixel.

Hausdorff distance (HD): Measures the maximum distance between predicted and ground truth surface points, capturing worst-case boundary errors:

$$d_H(A, B) = \max \left[\sup_{a \in A} \inf_{b \in B} d(a, b), \sup_{b \in B} \inf_{a \in A} d(b, a) \right] \quad (\text{C.2})$$

Where A and B are the sets of surface points from the predicted and ground truth masks, respectively, and \sup represents the supremum operator, \inf the infimum operator

Mean surface distance (MSD): Provides the average bidirectional boundary error which is less sensitive to outliers than the HD:

$$\text{MSD}(A, B) = \frac{1}{2} \left(\frac{1}{|A|} \sum_{a \in A} d(a, B) + \frac{1}{|B|} \sum_{b \in B} d(b, A) \right) \quad (\text{C.3})$$

Where:

- $|A|$ and $|B|$ are the number of points in sets A and B , respectively.
- $d(a, B) = \min_{b \in B} d(a, b)$
- $d(b, A) = \min_{a \in A} d(b, a)$

Appendix D. Practical training time (wall-clock)

Table D.5: Training resources and total GPU hours across models

Model	Training Resource*	Total GPU hours#
SAM ViT-B	~5 days @256 A100	~10,000
MedSAM	~21 days @20 A100	~10,000
SAMRI_{box}	~3 days @8 MI300X	608
SAMRI_{bp}	~3 days @8 MI300X	608

* Based on the original training dataset. # Standardized by $1 \times \text{GPU} / 1 \text{M training samples} / 100$ epochs. SAMRI_{box} denotes SAMRI with box-only prompts; SAMRI_{bp} denotes SAMRI with box+point prompts.

References

- Alom, M.Z., Yakopcic, C., Hasan, M., Taha, T.M., Asari, V.K., 2019. Recurrent residual u-net for medical image segmentation. *Journal of medical imaging* 6, 014006–014006.
- Azad, R., Aghdam, E.K., Rauland, A., Jia, Y., Avval, A.H., Bozorgpour, A., Karimijafarbigloo, S., Cohen, J.P., Adeli, E., Merhof, D., 2024. Medical image segmentation review: The success of u-net. *IEEE Transactions on Pattern Analysis and Machine Intelligence* 46, 10076–10095. doi:10.1109/TPAMI.2024.3435571.
- Cabezas, M., Oliver, A., Lladó, X., Freixenet, J., Cuadra, M.B., 2011. A review of atlas-based segmentation for magnetic resonance brain images. *Computer methods and programs in biomedicine* 104, e158–e177.
- Chandra, S.S., Dowling, J.A., Shen, K.K., Raniga, P., Pluim, J.P.W., Greer, P.B., Salvado, O., Fripp, J., 2012. Patient specific prostate segmentation in 3-d magnetic resonance images. *IEEE Transactions on Medical Imaging* 31, 1955–1964. doi:10.1109/TMI.2012.2211377.
- Chen, C., Miao, J., Wu, D., Zhong, A., Yan, Z., Kim, S., Hu, J., Liu, Z., Sun, L., Li, X., 2024. Ma-sam: Modality-agnostic sam adaptation for 3d medical image segmentation. *Medical Image Analysis* 98, 103310.

- Chua, L.O., 1997. Cnn: A vision of complexity. *International Journal of Bifurcation and Chaos* 07, 2219–2425. URL: <https://www.worldscientific.com/doi/abs/10.1142/S0218127497001618>, doi:10.1142/s0218127497001618.
- Çiçek, Ö., Abdulkadir, A., Lienkamp, S.S., Brox, T., Ronneberger, O., 2016. 3d u-net: learning dense volumetric segmentation from sparse annotation, in: *International conference on medical image computing and computer-assisted intervention*, Springer. pp. 424–432.
- Dai, W., Woo, B., Liu, S., Marques, M., Engstrom, C., Greer, P.B., Crozier, S., Dowling, J.A., Chandra, S.S., 2022. Can3d: Fast 3d medical image segmentation via compact context aggregation. *Medical Image Analysis* 82, 102562.
- Deng, X., Wu, H., Zeng, R., Qin, J., 2024. Memsam: Taming segment anything model for echocardiography video segmentation. *2024 IEEE/CVF Conference on Computer Vision and Pattern Recognition (CVPR)* doi:10.1109/CVPR52733.2024.00919.
- Despotović I, Goossens B, P.W., 2015. Mri segmentation of the human brain: challenges, methods, and applications. *Comput Math Methods Med* , 450341doi:10.1155/2015/450341.
- Dice, L.R., 1945. Measures of the amount of ecologic association between species. *Ecology* 26, 297–302.
- Dong, G., Wang, Z., Chen, Y., Sun, Y., Song, H., Liu, L., Cui, H., 2024. An efficient segment anything model for the segmentation of medical images. *Scientific Reports* 14, 19425.
- Dowling, J.A., Sun, J., Pichler, P., Rivest-Hénault, D., Ghose, S., Richardson, H., Wratten, C., Martin, J., Arm, J., Best, L., Chandra, S.S., Fripp, J., Menk, F.W., Greer, P.B., 2015. Automatic substitute computed tomography generation and contouring for magnetic resonance imaging (mri)-alone external beam radiation therapy from standard mri sequences. *International Journal of Radiation Oncology*Biophysics*Physics* 93, 1144–1153. URL: <https://www.sciencedirect.com/science/article/pii/S0360301615032472>, doi:<https://doi.org/10.1016/j.ijrobp.2015.08.045>.
- Fernandes, S.L., Tanik, U.J., Rajinikanth, V., Karthik, K.A., 2020. A reliable framework for accurate brain image examination and treatment planning based on early diagnosis support for clinicians. *Neural Computing and Applications* 32, 15897–15908. URL: <https://doi.org/10.1007/s00521-019-04369-5>, doi:10.1007/s00521-019-04369-5.
- Filippi, M., Agosta, F., 2007. Magnetization transfer mri in multiple sclerosis. *Journal of Neuroimaging* 17, 22S–26S.
- Finnis, K.W., Starreveld, Y.P., Parrent, A.G., Sadikot, A.F., Peters, T.M., 2002. Application of a population based electrophysiological database to the planning and guidance of deep brain stereotactic neurosurgery, in: Dohi, T., Kikinis, R. (Eds.), *Medical Image Computing and Computer-Assisted Intervention — MICCAI 2002*, Springer Berlin Heidelberg. pp. 69–76.
- Gao, Y., Xia, W., Hu, D., Wang, W., Gao, X., 2024. Desam: Decoupled segment anything model for generalizable medical image segmentation, in: *International Conference on Medical Image Computing and Computer-Assisted Intervention*, Springer. pp. 509–519.
- Haacke, E.M., Chen, Y., Utriainen, D., Wu, B., Wang, Y., Xia, S., He, N., Zhang, C., Wang, X., Lagana, M.M., Luo, Y., Fatemi, A., Liu, S., Gharabaghi, S., Wu, D., Sethi, S.K., Huang, F., Sun, T., Qu, F., Yadav, B.K., Ma, X., Bai, Y., Wang, M., Cheng, J., Yan, F., 2020. Strategically acquired gradient echo (stage) imaging, part iii: Technical advances and clinical applications of a rapid multi-contrast multi-parametric brain imaging method. *Magnetic Resonance Imaging* 65, 15–26. URL: <https://www.sciencedirect.com/science/article/pii/S0730725X19303820>, doi:<https://doi.org/10.1016/j.mri.2019.09.006>.
- Harada, T., Kudo, K., Fujima, N., Yoshikawa, M., Ikebe, Y., Sato, R., Shirai, T., Bito, Y., Uwano, I., Miyata, M., 2022. Quantitative susceptibility mapping: basic methods and clinical applications. *Radiographics* 42, 1161–1176.
- Harirpoush, A., Rasoulia, A., Kersten-Oertel, M., Xiao, Y., 2024. Architecture analysis and benchmarking of 3d u-shaped deep learning models for thoracic anatomical segmentation. *IEEE Access* 12, 127592–127603. doi:10.1109/ACCESS.2024.3456674.
- He, K., Chen, X., Xie, S., Li, Y., Dollár, P., Girshick, R., 2022. Masked autoencoders are scalable vision learners. *Proceedings of the IEEE/CVF conference on computer vision and pattern recognition* , 16000–16009.
- Huang, Y., Yang, X., Liu, L., Zhou, H., Chang, A., Zhou, X., Chen, R., Yu, J., Chen, J., Chen, C., Liu, S., Chi, H., Hu, X., Yue, K., Li, L., Grau, V., Fan, D.P., Dong, F., Ni, D., 2024. Segment anything model for medical images? *Medical Image Analysis* 92, 103061. URL: <https://www.sciencedirect.com/science/article/pii/S1361841523003213>, doi:<https://doi.org/10.1016/j.media.2023.103061>.
- Isensee, F., Petersen, J., Klein, A., Zimmerer, D., Jaeger, P.F., Kohl, S., Wasserthal, J., Koehler, G., Norajitra, T., Wirkert, S., 2018. nnu-net: Self-adapting framework for u-net-based medical image segmentation. *arXiv preprint arXiv:1809.10486* .
- Jager, F., Hornegger, J., 2009. Nonrigid registration of joint histograms for intensity standardization in magnetic resonance imaging. *IEEE Transactions on Medical Imaging* 28, 137–150. doi:10.1109/TMI.2008.2004429.

- Joskowicz, L., Cohen, D., Caplan, N., Sosna, J., 2019. Inter-observer variability of manual contour delineation of structures in ct. *European Radiology* 29, 1391–1399. URL: <https://doi.org/10.1007/s00330-018-5695-5>, doi:10.1007/s00330-018-5695-5.
- Kirillov, A., Mintun, E., Ravi, N., Mao, H., Rolland, C., Gustafson, L., Xiao, T., Whitehead, S., Berg, A.C., Lo, W.Y., 2023. Segment anything, in: *Proceedings of the IEEE/CVF international conference on computer vision*, pp. 4015–4026.
- Kraff, O., Fischer, A., Nagel, A.M., Mönninghoff, C., Ladd, M.E., 2015. Mri at 7 tesla and above: demonstrated and potential capabilities. *Journal of Magnetic Resonance Imaging* 41, 13–33.
- Kushol, R., Parnianpour, P., Wilman, A.H., Kalra, S., Yang, Y.H., 2023. Effects of mri scanner manufacturers in classification tasks with deep learning models. *Scientific Reports* 13, 16791. URL: <https://doi.org/10.1038/s41598-023-43715-5>, doi:10.1038/s41598-023-43715-5.
- Lee, H.H., Gu, Y., Zhao, T., Xu, Y., Yang, J., Usuyama, N., Wong, C., Wei, M., Landman, B.A., Huo, Y., 2024. Foundation models for biomedical image segmentation: A survey. *arXiv preprint arXiv:2401.07654*.
- Lei, W., Xu, W., Li, K., Zhang, X., Zhang, S., 2025. Medlsam: Localize and segment anything model for 3d ct images. *Medical Image Analysis* 99, 103370.
- Li, W., Hsu, C.Y., Wang, S., Yang, Y., Lee, H., Liljedahl, A., Witharana, C., Yang, Y., Rogers, B.M., Arundel, S.T., Jones, M.B., McHenry, K., Solis, P., 2024. Segment anything model can not segment anything: Assessing ai foundation model’s generalizability in permafrost mapping. *Remote Sensing* 16, 797. URL: <https://www.mdpi.com/2072-4292/16/5/797>.
- Lin, T.Y., Goyal, P., Girshick, R., He, K., Dollár, P., . Focal loss for dense object detection, in: *Proceedings of the IEEE international conference on computer vision*, pp. 2980–2988.
- Ma, J., He, Y., Li, F., Han, L., You, C., Wang, B., 2024. Segment anything in medical images. *Nature Communications* 15, 654. URL: <https://doi.org/10.1038/s41467-024-44824-z>, doi:10.1038/s41467-024-44824-z.
- Mazurowski, M.A., Dong, H., Gu, H., Yang, J., Konz, N., Zhang, Y., 2023. Segment anything model for medical image analysis: an experimental study. *Medical Image Analysis* 89, 102918.
- Milletari, F., Navab, N., Ahmadi, S.A., . V-net: Fully convolutional neural networks for volumetric medical image segmentation, in: *2016 fourth international conference on 3D vision (3DV)*, Ieee. pp. 565–571.
- Noh S, L.B., 2025. A narrative review of foundation models for medical image segmentation: zero-shot performance evaluation on diverse modalities. *Quant Imaging Med* doi:10.21037/qims-2024-2826.
- Nomura, Y., Hanaoka, S., Hayashi, N., Yoshikawa, T., Koshino, S., Sato, C., Tatsuta, M., Tanaka, Y., Kano, S., Nakaya, M., Inui, S., Kusakabe, M., Nakao, T., Miki, S., Watadani, T., Nakaoka, R., Shimizu, A., Abe, O., 2024. Performance changes due to differences among annotating radiologists for training data in computerized lesion detection. *International Journal of Computer Assisted Radiology and Surgery* 19, 1527–1536. URL: <https://doi.org/10.1007/s11548-024-03136-9>, doi:10.1007/s11548-024-03136-9.
- Nouman, M., Khoriba, G., Rashed, E.A., 2024. Rethinking medsam: Performance discrepancies in clinical applications. *2024 IEEE International Conference on Future Machine Learning and Data Science (FMLDS)* , 301–307doi:10.1109/FMLDS63805.2024.00061.
- Nouranian, S., Mahdavi, S.S., Spadinger, I., Morris, W.J., Salcudean, S.E., Abolmaesumi, P., 2015. A multi-atlas-based segmentation framework for prostate brachytherapy. *IEEE Transactions on Medical Imaging* 34, 950–961. doi:10.1109/TMI.2014.2371823.
- Oktay, O., Schlemper, J., Folgoc, L.L., Lee, M., Heinrich, M., Misawa, K., Mori, K., McDonagh, S., Hammerla, N.Y., Kainz, B., 2018. Attention u-net: Learning where to look for the pancreas. *arXiv preprint arXiv:1804.03999*.
- Pont-Tuset, J., Van Gool, L., . Boosting object proposals: From pascal to coco, in: *Proceedings of the IEEE international conference on computer vision*, pp. 1546–1554.
- Ren, W., Tang, Y., Sun, Q., Zhao, C., Han, Q.L., 2024. Visual semantic segmentation based on few/zero-shot learning: An overview. *IEEE/CAA Journal of Automatica Sinica* 11, 1106–1126. doi:10.1109/JAS.2023.123207.
- Renard, F., Guedria, S., Palma, N.D., Vuillerme, N., 2020. Variability and reproducibility in deep learning for medical image segmentation. *Scientific Reports* 10, 13724. URL: <https://doi.org/10.1038/s41598-020-69920-0>, doi:10.1038/s41598-020-69920-0.
- Ronneberger, O., Fischer, P., Brox, T., 2015. U-net: Convolutional networks for biomedical image segmentation, in: *Medical Image Computing and Computer-Assisted Intervention – MICCAI 2015*, Springer International Publishing. pp. 234–241.
- Sack, I., 2023. Magnetic resonance elastography from fundamental soft-tissue mechanics to diagnostic imaging. *Nature Reviews Physics* 5, 25–42. URL: <https://doi.org/10.1038/s42254-022-00543-2>, doi:10.1038/s42254-022-00543-2.

- Salehi, A.W., Khan, S., Gupta, G., Alabdullah, B.I., Almjally, A., Alsolai, H., Siddiqui, T., Mellit, A., 2023. A study of cnn and transfer learning in medical imaging: Advantages, challenges, future scope. *Sustainability* 15, 5930. doi:doi:10.3390/su15075930.
- Springer, E., Dymerska, B., Cardoso, P.L., Robinson, S.D., Weisstanner, C., Wiest, R., Schmitt, B., Trattnig, S., 2016. Comparison of routine brain imaging at 3 t and 7 t. *Investigative Radiology* 51. URL: https://journals.lww.com/investigativeradiology/fulltext/2016/08000/comparison_of_routine_brain_imaging_at_3_t_and_7_t.1.aspx.
- Stringer, C., Wang, T., Michaelos, M., Pachitariu, M., 2021. Cellpose: a generalist algorithm for cellular segmentation. *Nature Methods* 18, 100–106. URL: <https://doi.org/10.1038/s41592-020-01018-x>, doi:10.1038/s41592-020-01018-x.
- Sudre, C.H., Li, W., Vercauteren, T., Ourselin, S., Jorge Cardoso, M., . Generalised dice overlap as a deep learning loss function for highly unbalanced segmentations, in: *Deep Learning in Medical Image Analysis and Multimodal Learning for Clinical Decision Support: Third International Workshop, DLMIA 2017, and 7th International Workshop, ML-CDS 2017, Held in Conjunction with MICCAI 2017, Québec City, QC, Canada, September 14, Proceedings 3*, Springer. pp. 240–248.
- Sun, J., Chen, K., He, Z., Ren, S., He, X., Liu, X., Peng, C., 2024. Medical image analysis using improved sam-med2d: segmentation and classification perspectives. *BMC Medical Imaging* 24, 241.
- Trattnig, S., Hangel, G., Robinson, S.D., Juras, V., Szomolanyi, P., Dal-Bianco, A., 2024. Ultrahigh-field mri: where it really makes a difference. *Die Radiologie* 64, 1–8. URL: <https://doi.org/10.1007/s00117-023-01184-x>, doi:10.1007/s00117-023-01184-x.
- Wong, H.E., Rakic, M., Guttag, J., Dalca, A.V., 2024. Scribbleprompt: Fast and flexible interactive segmentation for any biomedical image. *Computer Vision – ECCV 2024*, 207–229.
- Wu, J., Wang, Z., Hong, M., Ji, W., Fu, H., Xu, Y., Xu, M., Jin, Y., 2025. Medical sam adapter: Adapting segment anything model for medical image segmentation. *Medical Image Analysis* 102, 103547. URL: <https://www.sciencedirect.com/science/article/pii/S1361841525000945>, doi:<https://doi.org/10.1016/j.media.2025.103547>.
- Yao, W., Bai, J., Liao, W., Chen, Y., Liu, M., Xie, Y., 2024. From cnn to transformer: A review of medical image segmentation models. *Journal of Imaging Informatics in Medicine* 37, 1529–1547. URL: <https://doi.org/10.1007/s10278-024-00981-7>, doi:10.1007/s10278-024-00981-7.
- Zhang, J., Zhang, Y., Jin, Y., Xu, J., Xu, X., 2023. Mdu-net: Multi-scale densely connected u-net for biomedical image segmentation. *Health Information Science and Systems* 11, 13.
- Zhao, T., Gu, Y., Yang, J., Usuyama, N., Lee, H.H., Kiblawi, S., Naumann, T., Gao, J., Crabtree, A., Abel, J., Mounq-Wen, C., Piening, B., Bifulco, C., Wei, M., Poon, H., Wang, S., 2025. A foundation model for joint segmentation, detection and recognition of biomedical objects across nine modalities. *Nature Methods* 22.
- Zhu, Y., Tchetchenian, A., Yin, X., Liew, A., Song, Y., Meijering, E., . Ac-unet: Adaptive connection unet for white matter tract segmentation through neural architecture search, in: *2024 IEEE International Symposium on Biomedical Imaging (ISBI)*, pp. 1–5. doi:10.1109/ISBI56570.2024.10635404.